

Article

Tuning Photophysical Properties via Positional Isomerization of the Pyridine Ring in Donor–Acceptor-Structured Aggregation-Induced Emission Luminogens Based on Phenylmethylene Pyridineacetonitrile Derivatives

Haiya Sun ^{1,*} , Shuixin Chen ¹, Aiguo Zhong ², Rong Sun ¹, Jiajie Jin ¹, Jiahao Yang ¹, Dongzhi Liu ³, Junfeng Niu ¹ and Shengli Lu ^{1,*}

¹ Key Laboratory of Chemical and Biological Processing Technology for Farm Products of Zhejiang Province, School of Biological and Chemical Engineering, Zhejiang University of Science and Technology, Hangzhou 310023, China; chenshuixin02@163.com (S.C.); 115069@zust.edu.cn (R.S.); 1200450057@zust.edu.cn (J.J.); yjh19858872471@163.com (J.Y.); 103044@zust.edu.cn (J.N.)

² School of Pharmaceutical and Chemical Engineering, Taizhou University, Taizhou 318000, China; zhongaiguo@tzc.edu.cn

³ School of Chemical Engineering and Technology, Tianjin University, Tianjin 300072, China; dzliu@tju.edu.cn

* Correspondence: 119012@zust.edu.cn (H.S.); lushengli@zust.edu.cn (S.L.)

Abstract: A series of aggregation-induced emission (AIE)-featured phenylmethylene pyridineacetonitrile derivatives named *o*-DBCNPY ((*Z*)-3-(4-(di-*p*-tolylamino)phenyl)-2-(pyridin-2-yl)acrylonitrile), *m*-DBCNPY ((*Z*)-3-(4-(di-*p*-tolylamino)phenyl)-2-(pyridin-3-yl)acrylonitrile), and *p*-DBCNPY ((*Z*)-3-(4-(di-*p*-tolylamino)phenyl)-2-(pyridin-4-yl)acrylonitrile) have been synthesized by tuning the substitution position of the pyridine ring. The linkage manner of the pyridine ring had influences on the molecular configuration and conjugation, thus leading to different photophysical properties. The absorption and fluorescence emission peak showed a bathochromic shift when the linking position of the pyridine ring changed from the *meta* to the *ortho* and *para* position. Meanwhile, *o*-DBCNPY exhibited the highest fluorescence quantum yield of 0.81 and the longest fluorescence lifetime of 7.96 ns as a neat film among all three isomers. Moreover, non-doped organic light-emitting diodes (OLEDs) were assembled in which the molecules acted as the light-emitting layer. Due to the relatively prominent emission properties, the electroluminescence (EL) performance of the *o*-DBCNPY-based OLED was superior to those of the devices based on the other two isomers with an external quantum efficiency (EQE) of 4.31%. The results indicate that delicate molecular modulation of AIE molecules could endow them with improved photophysical properties, making them potential candidates for organic photoelectronic devices.

Keywords: aggregation-induced emission; phenylmethylene pyridineacetonitrile; positional isomerization; fluorescence emission; non-doped organic light-emitting diode



Citation: Sun, H.; Chen, S.; Zhong, A.; Sun, R.; Jin, J.; Yang, J.; Liu, D.; Niu, J.; Lu, S. Tuning Photophysical Properties via Positional Isomerization of the Pyridine Ring in Donor–Acceptor-Structured Aggregation-Induced Emission Luminogens Based on Phenylmethylene Pyridineacetonitrile Derivatives. *Molecules* **2023**, *28*, 3282. <https://doi.org/10.3390/molecules28073282>

Academic Editor: Grzegorz D. Sulka

Received: 15 March 2023

Revised: 31 March 2023

Accepted: 3 April 2023

Published: 6 April 2023



Copyright: © 2023 by the authors. Licensee MDPI, Basel, Switzerland. This article is an open access article distributed under the terms and conditions of the Creative Commons Attribution (CC BY) license (<https://creativecommons.org/licenses/by/4.0/>).

1. Introduction

In recent years, the solid-state luminescence of organic materials has drawn much attention due to the rapid development of optoelectronic devices and applications such as organic light emitting diodes (OLEDs) [1–3], optical sensors [4], stimuli responses, and anti-counterfeit printing [5]. However, many organic materials exhibit intense fluorescence emission in dilute solutions, while the emission is severely quenched in the aggregate state. This undesirable aggregation-caused quenching (ACQ) effect has, to a large extent, restricted the applications of organic fluorescence materials in the solid state [6,7]. Fortunately, molecules with aggregation-induced emission (AIE) characteristics, which were first reported in 2001 by Tang's group, have shown their superiority in terms of strong fluorescent emission and high photostability in the aggregate state [8–10]. The concept

of AIE describes a unique phenomenon in that some organic fluorophores are weakly or non-emissive in a molecularly dissolved state (dilute solution), but intensely emissive in aggregate (solid) states [11]. The mechanism responsible for the AIE phenomenon is currently considered to be the restriction of intramolecular motions (RIM) [12–14]. As such, AIE luminogens (AIEgens) are usually characterized by propeller-shaped peripheral intramolecular rotors [15] or twisted configurations [16].

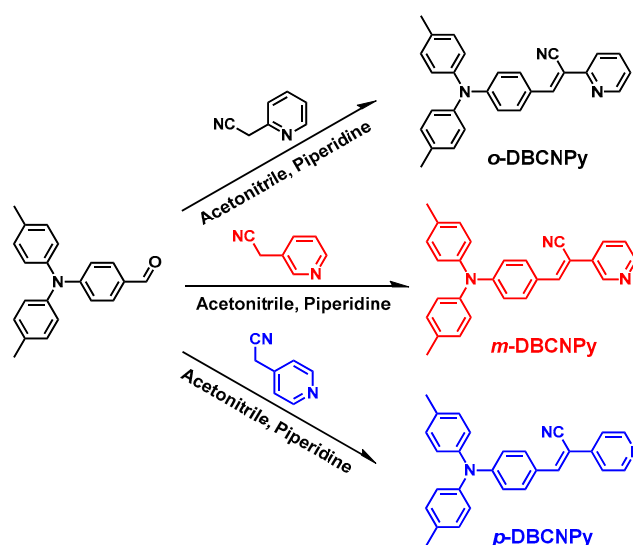
To date, several AIEgens, including silole [17], tetraphenylethene (TPE) [18], distyrylanthracene [19], tetraphenylpyrazine [20], quinoline-malononitrile [21], and cyanostilbene [22], have been reported. To exploit the fluorescence properties of AIEgens in aggregate states and to promote their application in solid-supported materials and devices, several strategies have been proposed in terms of molecular design. One strategy is to develop AIEgens with novel structures additional to the “traditional” silole and TPE core. For instance, chiral AIEgens based on 1,1'-bi-2-naphthol, metal complexes, and other chiral alkyl chains were reported and applied in circularly polarized organic light-emitting diodes (CPOLEDs) to pursue higher contrast and better emission efficiency in 3D displays [23]. Diarylethenes containing a benzobis(thiadiazole) linkage with large steric hindrance have been reported, of which some compounds show excellent potential for super-resolution imaging [24]. A series of organometallic or coordination AIEgens have been synthesized as mechanochromic luminescence (MCL) materials with better photophysical properties, richer emission colors, and more controllable MCL effects [25]. AIE polymers characterized by fused heterocyclic building blocks were also developed for the practical application of morphological structure visualization (e.g., microphase separation of polymer blends) and external stimuli response [26]. These research efforts have paved the way for the development of AIE-based optoelectronic devices, yet the synthetic complexity and material cost (such as the molecules containing noble metals) are currently the limitations for the broader applications of these AIEgens. Another strategy is the systematic structural tuning of the present AIEgens to optimize the solid-state luminescent properties. For organic fluorophores that are facilely modified, the substitution position effect of the functional groups or building blocks significantly affects the conjugation, intramolecular charge distribution, and transfer, and subsequently the photophysical properties [27–37]. Though some research has been performed that has provided the optimized substitution manner of the AIEgens, which led to the enhanced performance of the solid photoelectronic devices [38–40], more detailed investigations are still in demand to reveal and to further manipulate the detailed structure–property relationship.

To this end, a series of phenylmethylene pyridineacetonitrile derivatives bearing a triphenylamine (TPA) structure and pyridine ring with the nitrogen atom at the *ortho* (*o*-DBCNPY), *meta* (*m*-DBCNPY), and *para* (*p*-DBCNPY) position were designed and synthesized. The propeller-like TPA moiety was introduced as a strong electron donor and to prevent intimate π – π intermolecular stacking. The acceptor strength was tuned by varying the linking manner of the pyridyl ring. The photophysical properties of the compounds in solutions and the solid state were investigated. The emission performances in solid-state applications, including mechanofluorochromism and non-doped OLEDs, were studied and correlated to the substitutional position of the pyridyl group.

2. Results and Discussions

2.1. Synthesis and Characterization

The molecules were synthesized through Knoevenagel condensation between pyridinyl acetonitriles and 4-(di-*p*-tolylamino)benzaldehyde with yields of 65–75% (Scheme 1), and their structures were characterized by ^1H NMR, ^{13}C NMR, and HRMS (Figures S1–S6, Supplementary Materials). For solid fluorescence materials, thermal stability was a prerequisite before they were employed in the devices. Thermogravimetric analysis (TGA) results of the compounds are shown in Figure S7. The thermal decomposition temperatures (T_d , 5% weight loss) for *o*-DBCNPY, *m*-DBCNPY, and *p*-DBCNPY were 375 °C, 344 °C, and 343 °C, respectively, showing relatively good thermal stability.



Scheme 1. Synthetic routes of the compounds.

2.2. Spectral Analysis

Figure 1 shows the UV-vis absorption spectra of the compounds in solvents with different polarities. Two absorption peaks can be observed for all three molecules at around 295 nm and in the range of 400–420 nm: the former was ascribed to the TPA-localized electronic π - π^* transition [41,42], and the latter with a longer wavelength was due to the intramolecular charge transfer (ICT) resulting from electronic transition [43,44]. The absorption peak wavelength was barely shifted in the different solvents, indicating that the ground state charge transfer was hardly affected by the solvent polarity. Among the three molecules, *p*-DBCNP showed the most redshifted absorption peak, which was due to the increased conjugation between the *para*-pyridine and the TPA-acrylonitrile part [30]. Specifically, *p*-DBCNP had the largest absorption peak wavelength in THF (413 nm) in comparison to those of *o*-DBCNP (408 nm) and *m*-DBCNP (402 nm).

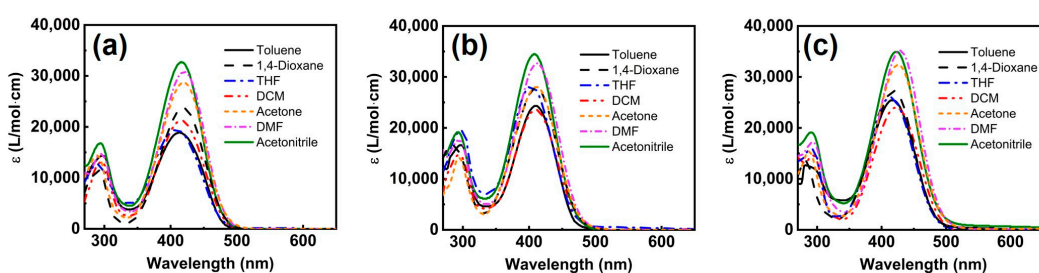


Figure 1. Absorption spectra of *o*-DBCNP (a), *m*-DBCNP (b), and *p*-DBCNP (c) in 1×10^{-5} M solutions (THF, tetrahydrofuran; DCM, dichloromethane; DMF, *N,N*-dimethylformamide).

The fluorescence emission spectra of the molecules are shown in Figure 2a–c. The solvent polarity had a large effect on the emission. On the one hand, a general trend was observed for all three fluorophores that the fluorescence emission peak was redshifted (62 nm for *o*-DBCNP, 57 nm for *m*-DBCNP, and 81 nm for *p*-DBCNP, respectively) and in the meantime, the emission intensity was diminished when the solvent polarity increased (from toluene to acetonitrile). The trend of increasing Stokes shift with the enhancement of the solvent polarity was also illustrated by the Lippert–Mataga model. As shown in Figure 2d, Stokes shifts of the molecules in different solvents rose linearly with a slope of over 5000 as the solvent orientation polarizability (Δf) grew, indicative of an obvious solvatochromic effect. On the other hand, the substituent positions of the pyridine ring also affected the emission property. For *p*-DBCNP, the best conjugation and the strongest

donor–acceptor interaction result in the most redshifted emission peak (566 nm in THF). In comparison, due to the less conjugated *meta*-linkage mode, the fluorescent emission peak wavelength was 25 nm shorter for *m*-DBCNPY in THF. The photophysical data of the isomers in THF are summarized in Table 1.

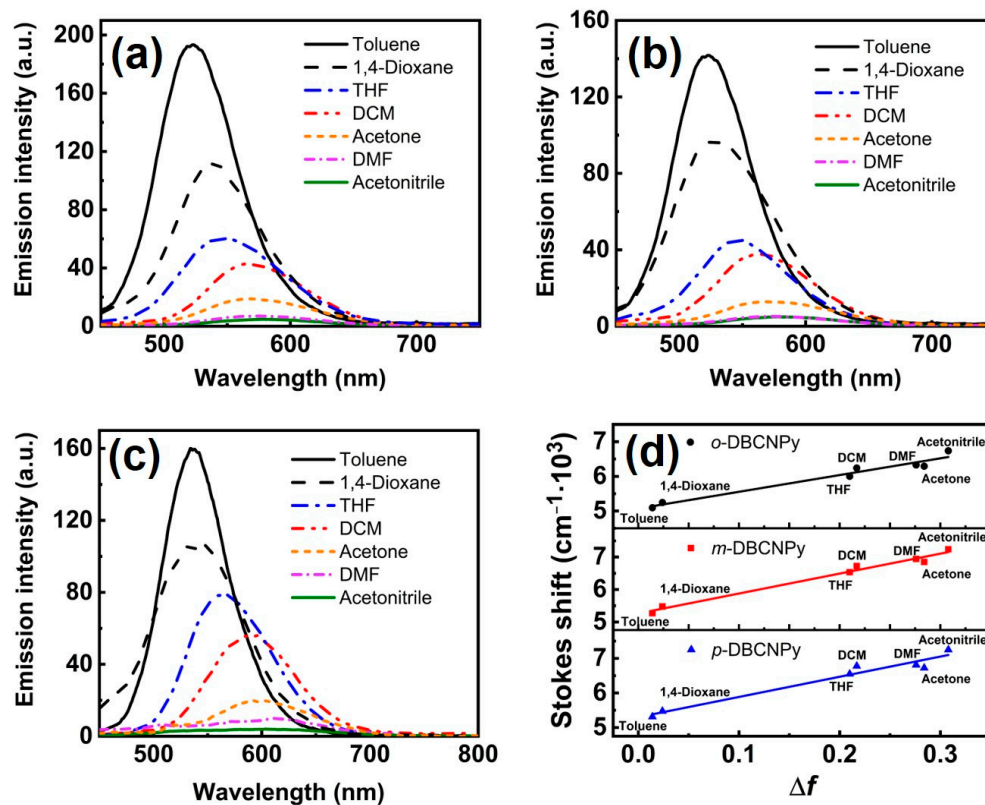


Figure 2. Fluorescence emission spectra of *o*-DBCNPY (a), *m*-DBCNPY (b), and *p*-DBCNPY (c) in 1×10^{-5} M solutions (THF, tetrahydrofuran; DCM, dichloromethane; DMF, *N,N*-dimethylformamide); the plot of Stokes shifts of the three isomers in different solvents versus solvent orientation polarizability (Δf) (d).

Table 1. Photophysical data of the isomers in 1×10^{-5} M THF solutions.

Compound	λ_{abs} (nm)	λ_{emi} (nm)	Stokes Shift (nm)	τ_f (ns)	$\Phi_{f,s}^a$	k_f^b (s ⁻¹)	k_{nr}^b (s ⁻¹)
<i>o</i> -DBCNPY	408	549	141	1.10	0.11	1.00×10^8	8.09×10^8
<i>m</i> -DBCNPY	402	541	139	0.85	0.10	1.18×10^8	1.06×10^9
<i>p</i> -DBCNPY	413	566	153	0.81	0.08	9.88×10^7	1.14×10^9

^a Fluorescence quantum yield in THF solutions. Rhodamine B (0.7 in ethanol) was used as the reference [18]. ^b k_f , radiative decay rate constant ($k_f = \Phi_{f,s} / \tau_f$); k_{nr} , nonradiative decay rate constant ($k_{nr} = 1 / \tau_f - k_f$) [43].

The photophysical properties of the molecules at solid state (as neat film) were investigated. Figure S8 shows that the absorption bands of the compound neat films were around 410 nm, and the emission peak wavelengths were slightly different (543 nm for *o*-DBCNPY, 541 nm for *m*-DBCNPY, and 548 nm for *p*-DBCNPY). The fluorescence lifetimes of the solid-state compounds were elongated in comparison to those in solutions (Figure 3). Specifically, the *o*-DBCNPY film showed the longest fluorescence lifetime of 7.96 ns, 7.2 times extended when compared to the emission lifetime in THF. Meanwhile, the fluorescence quantum yields of the neat films of all compounds ($\Phi_{f,f}$) were measured. *O*-DBCNPY film was highly emissive, with the $\Phi_{f,f}$ reaching 0.81, showing good potential as an organic light-emitting material. In comparison, *m*-DBCNPY showed the lowest $\Phi_{f,f}$ (0.49) among all three isomers, which was attributed to its short fluorescence lifetime. Overall, the enhanced emission intensity and the extended fluorescence lifetime of the

non-doped films indicates that the formation of the aggregate state may affect the decay pathway of the excited state, i.e., suppressing the nonradiative decay [45–47]. The different fluorescence lifetimes and quantum yields among the isomers were probably derived from the varied molecular configurations and conjugations in the solid state due to the substitutional position of the pyridine ring [48]. For *o*-DBCNPy, the strongest emission intensity might be derived from a more planarized molecular configuration led by the interaction between the *ortho*-nitrogen atom and the vinyl hydrogen atom (-CH=C-). The fluorescence emission data of the compound films are listed in Table 2.

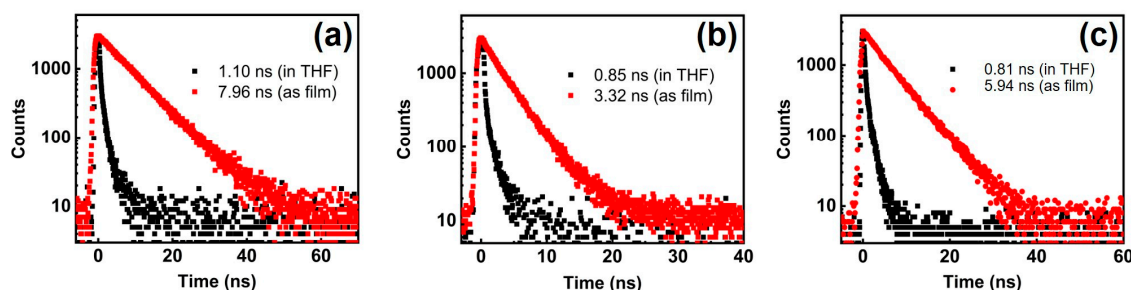


Figure 3. Fluorescence lifetimes of *o*-DBCNPy (a), *m*-DBCNPy (b), and *p*-DBCNPy (c) in THF and as neat film.

Table 2. Fluorescence properties of the neat films of the molecules.

Compound	λ_{emi} (nm)	τ_f^a (ns)	$\Phi_{f,f}^a$	k_f^b (s ⁻¹)	k_{nr}^b (s ⁻¹)
<i>o</i> -DBCNPy	543	7.96	0.81	1.02×10^8	2.36×10^7
<i>m</i> -DBCNPy	541	3.32	0.47	1.42×10^8	1.60×10^8
<i>p</i> -DBCNPy	549	5.94	0.57	9.60×10^7	7.24×10^7

^a Absolute fluorescence quantum yields of the films ($\Phi_{f,f}$) were obtained by a calibrated integrating sphere. ^b k_f , radiative decay rate constant ($k_f = \Phi_{f,s} / \tau_f$); k_{nr} , nonradiative decay rate constant ($k_{nr} = 1 / \tau_f - k_f$).

2.3. Aggregation-Induced Emission (AIE)

To understand the spectral properties of the compounds from solutions to aggregate state, the absorption and fluorescence emission spectra were recorded in the THF (good solvent)–water (poor solvent) mixtures with increasing water fractions (f_w , by volume %). As shown in Figure S9, the absorption of the compounds was barely affected when f_w was below 70%. When the water ratio further increased, the absorption band was redshifted with a level-off absorption tail extended to a longer wavelength. This was due to the Mie scattering by the nano-aggregates of the molecules at high f_w [49]. The fluorescence emission spectra of all isomers are shown in Figure 4a–c, and the variations in emission intensity and peak position with respect to the f_w are also shown in Figure 4d–f. As the f_w increased to 70–80%, the emission intensity steadily dropped with the fluorescence quantum yield in solution ($\Phi_{f,s}$), decreased to less than 0.02, and the emission maximum wavelength shifted bathochromatically. The diminished fluorescence emission can be explained by the twisted intramolecular charge transfer process of a typical donor–acceptor (D–A) fluorophore in solvents with high polarity [50]. The redshifted emission was due to solvatochromism. When f_w increased, the fluorescence emission was intensified drastically. At $f_w = 95\%$, the dispersions of the three molecules showed significantly increased $\Phi_{f,s}$ values of 0.25–0.34. This could be attributed to the formation of aggregates [47,51]. Considering that (1) the molecules were highly emissive in the solid state and (2) they showed significantly enhanced fluorescence emission during the aggregate formation, the DBCNPy isomers belonged to typical AIE molecules.

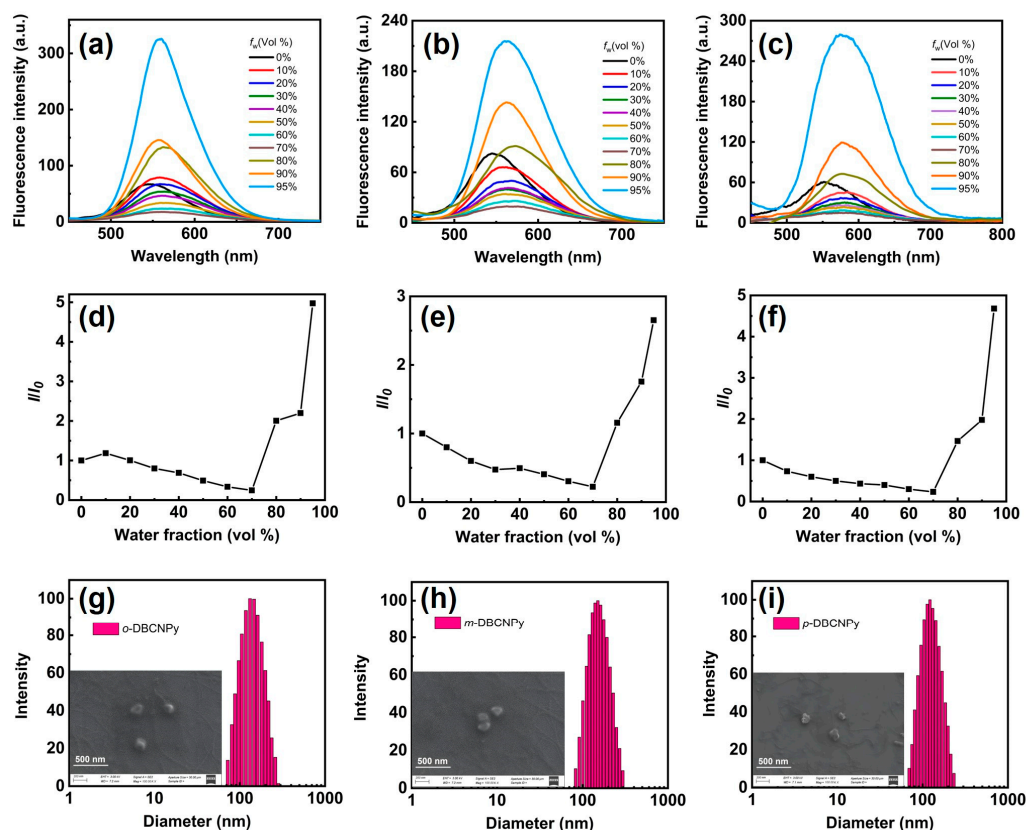


Figure 4. Fluorescence spectra, variation in relative emission intensity (I/I_0), and emission maxima wavelength of *o*-DBCNPY (a,d), *m*-DBCNPY (b,e), and *p*-DBCNPY (c,f) in THF–water mixtures with increasing f_w (concentration of compound: 1×10^{-5} M, $\lambda_{ex} = 415$ nm); size distributions of *o*-DBCNPY (g), *m*-DBCNPY (h), and *p*-DBCNPY (i) aggregates in THF–water mixtures ($f_w = 95\%$) (insets are SEM images of the particles).

Moreover, the formation of the nano-aggregates of the isomers in THF–water mixtures at high f_w is evidenced by the results from the dynamic light scattering (DLS) and scanning electron microscopy (SEM) characterizations. Figure 4g–i shows that the average sizes of the aggregates were within the range of 120–150 nm. The particles can also be observed in the inset SEM images, which support the DLS data.

2.4. Electronic Properties

To gain insight into the molecular structures and the electronic properties of the DBCNPY isomers, density functional theory (DFT) calculations were performed with the Gaussian 09 program at the B3LYP/6-311g(d) basis set [52]. The optimized molecular geometries (Figure 5) revealed the different planarities of the isomers' acceptor moieties. The torsion angle between the pyrimidine ring and the central $-C=C-$ plane increased from 11.22° in *p*-DBCNPY to 31.43° in *m*-DBCNPY, which was presumably due to the repulsion between the cyano group and the lone-pair electrons on the *meta*-nitrogen atom. In *o*-DBCNPY, however, the torsion angle was decreased to only 0.98° . This could be attributed to the interaction between the *ortho*-nitrogen atom and the hydrogen on the vinyl group ($-\text{CH}=\text{C}-$). The torsion extent of the pyridine ring in the three isomers might partly explain the differences in their fluorescence properties: higher planarity between the imide and the pyridine led to elongated fluorescence lifetime and more intense fluorescence emission. In addition, the distributions of the frontier molecular orbitals are also depicted in Figure 5. The highest occupied molecular orbitals (HOMOs) and lowest unoccupied molecular orbitals (LUMOs) of the isomers were spatially separated, with the former mainly located on the TPA moiety and

the latter distributed on the imide and pyridine part, demonstrating the D–A feature of the isomers [53].

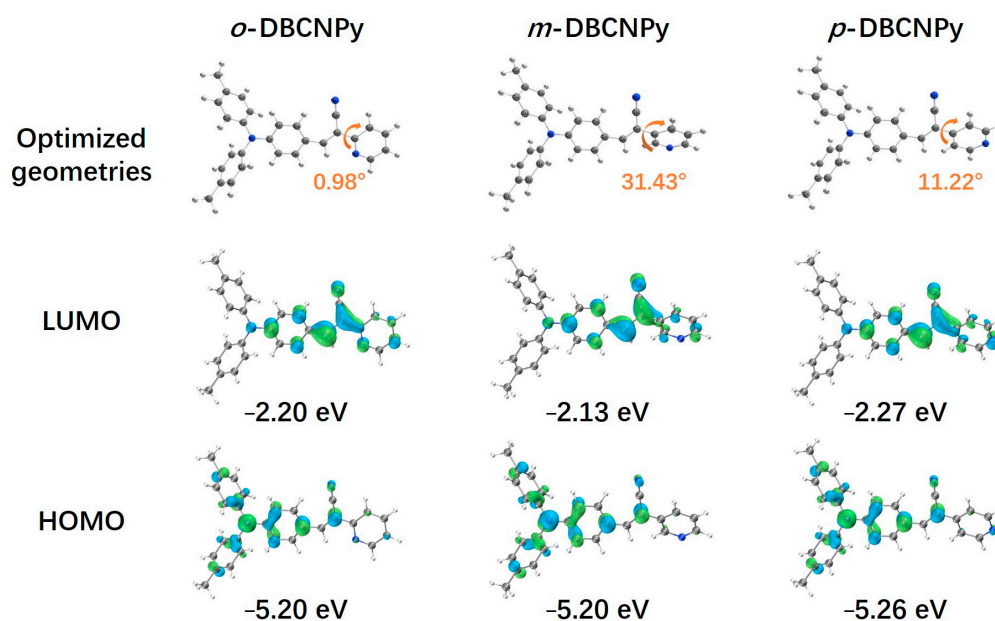


Figure 5. Optimized molecular geometries, electron density distributions, and energy levels of the HOMO and LUMO orbitals for the molecules at the B3LYP/6-311g(d) basis set.

Cyclic voltammetry (CV) analysis was carried out and the CV curves of the fluorophores were recorded (Figure 6). The oxidation potential (E_{ox}) of the three molecules from the quasi-reversible oxidation peak of the triphenylamine part were similar (0.60–0.62 V). The reduction potentials (E_{red}) showed a slight difference among the isomers, and were determined to be -1.98 V, -2.01 V, and -1.93 V for *o*-DBCNPY, *m*-DBCNPY, and *p*-DBCNPY, respectively. Accordingly, the vertical ionization potential (IP) and the vertical electron affinity (EA) were estimated by the equations $IP = 4.93 \text{ eV} + E_{ox}$ and $EA = 4.93 \text{ eV} + E_{red}$ [54,55], and the data are given in Table 3. The results indicate that the *para*-pyridine showed a stronger electron-accepting ability than the other two isomers. This is also in accordance with the results of the spectral analysis. Notably, the IP and EA values matched well with most of the hole- and electron-transporting materials, meaning that these isomers were energetically appropriate to be assembled into electroluminescence devices as emitting materials.

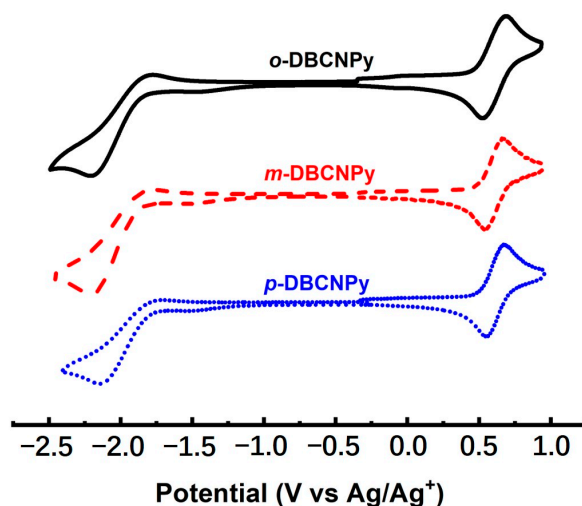


Figure 6. Cyclic voltammograms of the compounds; scan rate, 50 mV s^{-1} .

Table 3. Electrochemical data of the isomers.

Compound	E_{ox}^a (V)	E_{red}^a (V)	IP ^b (eV)	EA ^c (eV)
<i>o</i> -DBCNPY	0.60	−1.98	5.53	2.95
<i>m</i> -DBCNPY	0.62	−2.01	5.55	2.92
<i>p</i> -DBCNPY	0.61	−1.93	5.54	3.00

^a Oxidation (reduction) potential, estimated from the onset of the first oxidation (reduction) wave, V versus Ag/Ag⁺; ^b vertical ionization potential, IP = 4.93 eV + E_{ox} (the value (minus) 4.93 eV was obtained from the calibration of the Ag⁺ electrode versus vacuum) [44]; ^c vertical electron affinity, EA = 4.93 eV + E_{red} .

2.5. Mechanofluorochromism

Considering that *p*-DBCNPY was relatively sensitive toward the stimulus of external force, the mechanofluorochromic (MFC) properties of the other two isomers were also investigated, and their emission spectra and powder X-ray diffraction (XRD) patterns at different states are demonstrated in Figure 7. Unfortunately, the MFC effect of *o*-DBCNPY and *m*-DBCNPY was not as prominent as that of *p*-DBCNPY. Although *o*-DBCNPY and *m*-DBCNPY showed good reversibility during grinding and solvent fuming, the wavelength changes were no more than 20 nm. This was probably due to a smaller change in the powder morphology under external force: partially losing their crystallinity instead of fully converting into an amorphous form [56]. After hard grinding, the XRD patterns of *o*-DBCNPY and *m*-DBCNPY retained some features of a microcrystalline structure, as shown in Figure 7d,e. Furthermore, the differential scanning calorimetry (DSC) curves (Figure S10) show only weak exothermic peaks at 93.5 °C for *o*-DBCNPY and 99.7 °C for *m*-DBCNPY, indicative of a smaller extent of the cold crystallization process than that of *p*-DBCNPY [57]. Meanwhile, although attempts were made to grow single crystals of *o*-DBCNPY and *m*-DBCNPY, the needle-like crispy microcrystals were unable to be analyzed by single-crystal X-ray diffraction. In comparison, *p*-DBCNPY easily formed well-ordered microcrystals or even single crystals through slow solvent evaporation, and the orderly arranged molecules transformed into an amorphous state upon grinding (Figure 7f). The results indicate that the substitution position of the pyridine ring could affect the crystallinity and MFC property of the molecule series.

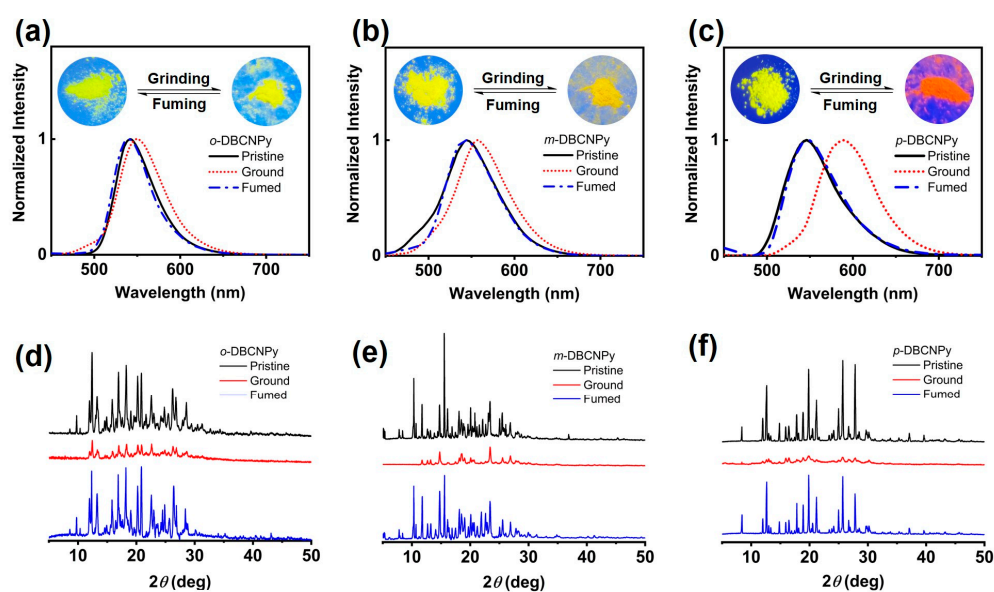


Figure 7. Fluorescence emission spectra and XRD patterns of *o*-DBCNPY (a,d), *m*-DBCNPY (b,e), and *p*-DBCNPY (c,f) when solid at various states (pristine, ground, and fumed); insets are images of the each solid under 365 nm UV light.

2.6. OLED Device Performances

Non-doped organic light-emitting diode (OLED) devices based on the three molecules were fabricated due to their relatively high fluorescence quantum yields in solid state (film) and appropriate IPs and EAs. The devices were assembled based on the following configuration: ITO/MoO₃ (hole injection layer, 3 nm)/TAPC (hole-transporting layer, 50 nm)/TCTA (exciton-blocking layer, 10 nm)/DBCNPY isomers (light-emitting layer, 25 nm)/TPBi (electron-transporting layer, 50 nm)/LiF (electron injection layer, 1 nm)/Al [58]. The electroluminescence (EL) characteristics of the devices are demonstrated in Figure 8, and the data are summarized in Table 4. All OLEDs emit green light with a brightness exceeding 2000 cd m⁻², and the light colors of the *o*-DBCNPY- and *m*-DBCNPY-based devices were close to pure green (color coordinates (0.21, 0.71)). The best electroluminescence performance was achieved by the device base on *o*-DBCNPY with a maximum current efficiency (CE), power efficiency (PE), and external quantum efficiency (EQE) of 18.95 cd A⁻¹, 15.76 lm W⁻¹, and 4.31%, respectively, and the color coordinates are (0.26, 0.70). By comparing the EL performances among the three devices, it was observed that the parameters (especially EQE) were roughly in accordance with the fluorescence quantum yields of the non-doped films ($\Phi_{f,f}$). In terms of EQE, the *o*-DBCNPY-based device was among the best of the traditional fluorescent OLEDs based on cyanostilbene derivatives reported so far [59,60], including doped and non-doped devices. In addition, the EL performances and the structural modification feasibility made it possible to produce white OLEDs using the DBCNPY molecule series as the emitting materials.

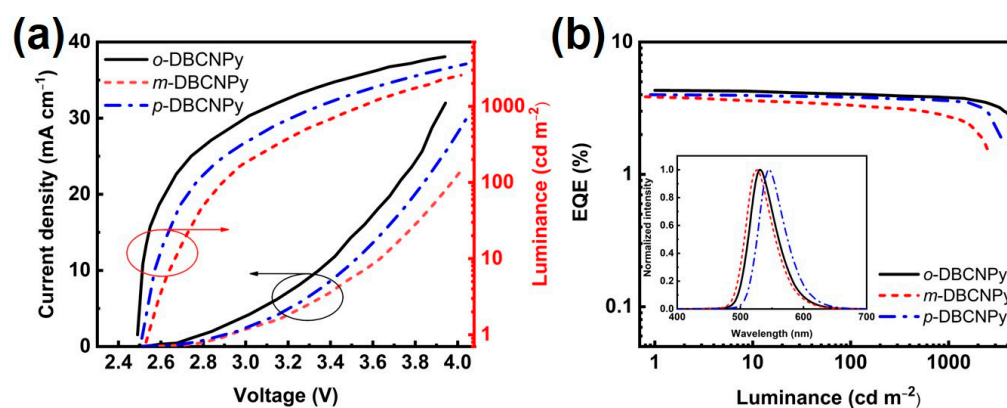


Figure 8. Current density–voltage–luminance (J – V – L) (a) and EQE–luminance characteristics (b) for the devices (inset showed the EL spectra).

Table 4. Electroluminescence (EL) performance of non-doped OLEDs based on the molecules.

Devices	Maximum Brightness (cd m ⁻²)	Maximum Current Efficiency (CE) (cd A ⁻¹)	Maximum Power Efficiency (PE) (lm W ⁻¹)	Maximum External Quantum Efficiency (EQE) (%)	CIE Coordinates
<i>o</i> -DBCNPY	4487	18.95	15.76	4.31	0.26, 0.70
<i>m</i> -DBCNPY	2561	14.32	11.54	3.25	0.25, 0.71
<i>p</i> -DBCNPY	3604	16.88	14.59	3.99	0.29, 0.67

3. Materials and Methods

3.1. Materials and Characterization

Starting materials including the donor molecule 4-(di-*p*-tolylamino)benzaldehyde, the acceptor building block 2-(pyridin-2-yl)acetonitrile, 3-(pyridin-2-yl)acetonitrile, 4-(pyridin-2-yl)acetonitrile, and MoO₃, LiF, 4,4'-cyclohexylidene bis[*N,N*-bis(*p*-tolyl)aniline] (TAPC), 1,3,5-tris(1-phenyl-1*H*-benzimidazol-2-yl)benzene (TPBi), and 4,4',4''-tris(carbazol-9-yl)-triphenylamine (TCTA) for device fabrication were obtained from Energy Chemical (Shang-

hai, China), Bide Pharmatech Co., Ltd. (Shanghai, China) and Aladdin Biochemical Technology Co., Ltd. (Shanghai, China), and were used without further treatment. All solvents were of AR grade and were purified by the established procedures.

Nuclear magnetic resonance measurements, including ^1H NMR (400 MHz) and ^{13}C NMR (100 MHz), were performed on Bruker spectrometers at 25 °C. High-resolution mass spectroscopy (HRMS) analysis was performed on a Bruker micrOTOF-Q II mass spectrometer. For spectral analysis, the absorption and fluorescence emission spectra were acquired on a Bruker UV/vis spectrometer and a Bruker fluorescence spectrophotometer, respectively. Time-resolved fluorescence analysis and fluorescence quantum yield measurements were carried out on an Edinburgh FLS1000 (Livingston, UK) fluorescence spectrophotometer. For nano-aggregates, the particle size was measured through dynamic light scattering (DLS) measurements via a Malvern Zetasizer Nano ZS90 (Malvern Panalytical, Malvern, UK) size analyzer and observed using a Zeiss Sigma 300 (Jena, Germany) scanning electron microscope (SEM). The microcrystalline structure of the compounds was analyzed via an X-ray diffraction (XRD) SmartLab (Rigaku, Tokyo, Japan) X-ray diffractometer at room temperature.

3.2. Synthesis

General synthetic method of the molecules. The target compounds were synthesized according to a previous report [57]. Briefly, 4-(di-*p*-tolylamino)benzaldehyde (1 equiv.) and (pyridin-2-yl)acetonitrile derivatives (1.2 equiv.) were dissolved in 20–30 mL acetonitrile, and a catalytic amount of piperidine (usually three drops per mmol of the reactant) was added into the solution. The reactant mixture was stirred at 85 °C for 8–10 h and was then filtered. The precipitate was rinsed with cold ethanol and recrystallized in a mixed solvent of cyclohexane and dichloromethane (10:1–15:1, *v/v*).

Synthesis and characterization of (Z)-3-(4-(di-*p*-tolylamino)phenyl)-2-(pyridin-2-yl)acrylonitrile (***o*-DBCNPY**). ***o*-DBCNPY** was obtained as a bright yellow solid from the starting material 4-(di-*p*-tolylamino)benzaldehyde and 2-(pyridin-2-yl)acetonitrile (yield: 71%). ^1H NMR (400 MHz, CDCl_3 , δ): 8.60 (d, $J = 4.4$ Hz, 1H), 8.34 (s, 1H), 7.85 (d, $J = 8.8$ Hz, 2H), 7.77–7.69 (m, 2H), 7.23–7.20 (m, 1H), 7.13 (d, $J = 8.4$ Hz, 4H), 7.07 (d, $J = 8.4$ Hz, 4H), 6.97 (d, $J = 8.8$ Hz, 2H), 2.34 (s, 6H). ^{13}C NMR (100 MHz, CDCl_3 , δ): 152.02, 150.96, 149.46, 144.62, 143.82, 137.24, 134.53, 131.61, 130.26, 126.10, 125.00, 122.62, 120.76, 119.23, 118.88, 105.18, 20.96. HRMS (ESI) m/z : $[\text{M} + \text{H}]^+$ calcd for $\text{C}_{28}\text{H}_{23}\text{N}_3$, 402.1965; found, 402.1961.

Synthesis and characterization of (Z)-3-(4-(di-*p*-tolylamino)phenyl)-2-(pyridin-3-yl)acrylonitrile (***m*-DBCNPY**). ***m*-DBCNPY** was acquired as a pale yellow solid from 4-(di-*p*-tolylamino)benzaldehyde and 3-(pyridin-2-yl)acetonitrile (yield: 66%). ^1H NMR (40 MHz, CDCl_3 , δ): 8.88 (d, $J = 2.0$ Hz, 1H), 8.57 (d, $J = 4.8$ Hz, 1H), 7.92 (d, $J = 8.0$ Hz, 1H), 7.76 (d, $J = 8.8$ Hz, 2H), 7.42 (s, 1H), 7.36–7.30 (m, 1H), 7.14 (d, $J = 8.4$ Hz, 4H), 7.07 (d, $J = 8.4$ Hz, 4H), 6.98 (d, $J = 8.8$ Hz, 2H), 2.35 (s, 6H). ^{13}C NMR (100 MHz, CDCl_3 , δ): 150.91, 149.22, 146.78, 143.77, 143.28, 134.59, 133.00, 131.38, 130.98, 130.28, 126.06, 124.86, 123.54, 119.31, 118.22, 103.19, 20.96. HRMS (ESI) m/z : $[\text{M} + \text{H}]^+$ calcd for $\text{C}_{28}\text{H}_{23}\text{N}_3$, 402.1965; found, 402.1959.

Synthesis and characterization of (Z)-3-(4-(di-*p*-tolylamino)phenyl)-2-(pyridin-4-yl)acrylonitrile (***p*-DBCNPY**). ***p*-DBCNPY** was obtained as a bright yellow crystal from 4-(di-*p*-tolylamino)benzaldehyde and 4-(pyridin-2-yl)acetonitrile (yield: 75%). The characterization data have been reported by [57].

3.3. Electrochemical Measurement

The CHI 660E Electrochemical Workstation was used to conduct the measurements of the electrochemical properties. A three-electrode set up, calibrated by utilizing the ferrocene/ferrocenium (Fc/Fc^+) redox couple, was used in the measurements. The Ag/AgNO_3 electrode was chosen as the reference electrode. Tetra-butyl ammonium hexafluorophosphate (TBAPF_6) was dissolved in dichloromethane (0.1 M) as the electrolyte.

3.4. Fabrication and Characterization of Electroluminescent Devices

Indium tin oxide (ITO) conducting glass was washed, cleaned ultrasonically, and treated with ultraviolet and ozone prior to use. The compounds were sublimated at the condition of 200 °C and 1×10^{-3} Pa. The light-emitting layer, electron/hole transport layer, and electrode were deposited onto the ITO substrates at a pressure of 5×10^{-4} Pa. The electroluminescence characteristics and the emission spectra of the devices were measured by a Keithley 2400 (Tektronix, Inc., Beaverton, OR, USA) source meter and a PR655 (North Syracuse, NY, USA) SpectraScan[®] spectrometer.

4. Conclusions

In conclusion, three phenylmethylene pyridineacetonitrile derivatives (*o*-DBCNPY, *m*-DBCNPY, and *p*-DBCNPY) with various substitution positions of the pyridine ring have been synthesized via Knoevenagel condensation in good yields. All three compounds were characterized with aggregation-induced emission (AIE) features since they were highly emissive in the solid state and their fluorescence emission showed significant enhancement during aggregate formation. The positional isomerization of the pyridine ring has affected the configuration and conjugation of the molecules, resulting in different photophysical properties. From *m*-DBCNPY to *o*-DBCNPY and to *p*-DBCNPY, the absorption and fluorescence emission peaks were bathochromically shifted in solutions and as neat films due to the enhanced intramolecular conjugation. Especially, *o*-DBCNPY exhibited the highest fluorescence quantum yield of 0.81 and the longest fluorescence lifetime of 7.96 ns as neat film of all three isomers. Moreover, non-doped organic OLEDs were fabricated using the molecules as the light-emitting layer. The best EL performance of all devices was achieved by the one based on *o*-DBCNPY. The maximum CE, PE, and EQE were 18.95 cd A⁻¹, 15.76 lm W⁻¹, and 4.31%, respectively, with color coordinates of (0.26, 0.70), which were close to that of the pure green color. The EL performances were mainly derived from the high fluorescence quantum yield of the *o*-DBCNPY neat film. Therefore, the delicate molecular tuning of AIEgens could provide them with enhanced photophysical properties, which makes them promising candidates for organic photoelectronic devices.

Supplementary Materials: The following supporting information can be downloaded at <https://www.mdpi.com/article/10.3390/molecules28073282/s1>. Figure S1: ¹H NMR (400 MHz, CDCl₃) spectrum of compound *o*-DBCNPY; Figure S2: ¹³C NMR (100 MHz, CDCl₃) spectrum of compound *o*-DBCNPY; Figure S3: HRMS spectrum of compound *o*-DBCNPY; Figure S4: ¹H NMR (400 MHz, CDCl₃) spectrum of compound *m*-DBCNPY; Figure S5: ¹³C NMR (100 MHz, CDCl₃) spectrum of compound *m*-DBCNPY; Figure S6: HRMS spectrum of compound *m*-DBCNPY; Figure S7: TGA curves of *o*-DBCNPY, *m*-DBCNPY, and *p*-DBCNPY; Figure S8: Absorption (a) and fluorescence emission (b) spectra of the non-doped film of the compounds; Figure S9: Absorption spectra of *o*-DBCNPY (a), *m*-DBCNPY (b), and *p*-DBCNPY (c) in THF/water mixtures. Concentration: 1×10^{-5} M; Figure S10: DSC curves of *o*-DBCNPY (a) and *m*-DBCNPY (b) in different states.

Author Contributions: Conceptualization, H.S. and J.N.; methodology, H.S. and D.L.; investigation, A.Z., J.J. and J.Y.; resources, A.Z. and R.S.; data curation, S.C.; writing—original draft preparation, H.S.; writing—review and editing, S.C. and S.L.; supervision, S.L.; funding acquisition, H.S., R.S. and J.N. All authors have read and agreed to the published version of the manuscript.

Funding: This research was funded by the National Natural Science Foundation of China (Grant No. 22105171), the Natural Science Foundation of Zhejiang Province (LQ20B020002 and LQ19E030001), Key R&D Project for Tackling Key Scientific and Technological Problems of Zhejiang Province, the “Leading Swan Goose Project” (2022C01177), and Zhejiang Administration for Market Regulation Eyas Program Cultivation Project (CY2022355).

Institutional Review Board Statement: Not applicable.

Informed Consent Statement: Not applicable.

Data Availability Statement: The data presented in this study are available in the Supplementary Materials.

Conflicts of Interest: The authors declare no conflict of interest.

Sample Availability: Samples of the compounds *o*-DBCNPY, *m*-DBCNPY, and *p*-DBCNPY are available from the authors.

References

1. Meng, S.-G.; Zhu, X.-Z.; Zhou, D.-Y.; Liao, L.-S. Recent Progresses in Solution-Processed Tandem Organic and Quantum Dots Light-Emitting Diodes. *Molecules* **2023**, *28*, 134. [[CrossRef](#)] [[PubMed](#)]
2. Fei, N.; Wei, Q.; Cao, L.; Bai, Y.; Ji, H.L.; Peng, R.X.; Huang, L.; Hao, S.Y.; Ge, Z.Y. A symmetric nonpolar blue AIEgen as nondoped fluorescent OLED emitter with low efficiency roll-off. *Org. Electron.* **2020**, *78*, 105574. [[CrossRef](#)]
3. Xu, Y.; Xu, P.; Hu, D.; Ma, Y. Recent progress in hot exciton materials for organic light-emitting diodes. *Chem. Soc. Rev.* **2021**, *50*, 1030. [[CrossRef](#)] [[PubMed](#)]
4. Diana, R.; Caruso, U.; Gentile, F.S.; Di Costanzo, L.; Panunzi, B. A Novel L-Shaped Fluorescent Probe for AIE Sensing of Zinc (II) Ion by a DR/NIR Response. *Molecules* **2021**, *26*, 7347. [[CrossRef](#)]
5. Liu, R.R.; Jing, J.B.; Zhang, S.; Wang, K.; Tian, W.J.; Yang, P. Aggregation-induced emission of a 2D protein supramolecular nanofilm with emergent functions. *Mater. Chem. Front.* **2020**, *4*, 1256. [[CrossRef](#)]
6. Mei, J.; Leung, N.L.C.; Kwok, R.T.K.; Lam, J.W.Y.; Tang, B.Z. Aggregation-Induced Emission: Together We Shine, United We Soar! *Chem. Rev.* **2015**, *115*, 11718–11940. [[CrossRef](#)]
7. Huang, S.; Shan, G.; Qin, C.; Liu, S. Polymerization-Enhanced Photophysical Performances of AIEgens for Chemo/Bio-Sensing and Therapy. *Molecules* **2023**, *28*, 78. [[CrossRef](#)]
8. Luo, J.; Xie, Z.; Lam, J.W.Y.; Cheng, L.; Chen, H.; Qiu, C.; Kwok, H.S.; Zhan, X.; Liu, Y.; Zhu, D.; et al. Aggregation-induced emission of 1-methyl-1,2,3,4,5-pentaphenylsilole. *Chem. Commun.* **2001**, *18*, 1740. [[CrossRef](#)]
9. Hong, Y.; Lam, J.W.Y.; Tang, B.Z. Aggregation-induced emission: Phenomenon, mechanism and applications. *Chem. Commun.* **2009**, *29*, 4332. [[CrossRef](#)]
10. Hong, Y.; Lam, J.W.Y.; Tang, B.Z. Aggregation-induced emission. *Chem. Soc. Rev.* **2011**, *40*, 5361. [[CrossRef](#)]
11. Pramanik, B.; Das, D. Aggregation-Induced Emission or Hydrolysis by Water? the Case of Schiff Bases in Aqueous Organic Solvents. *J. Phys. Chem. C* **2018**, *122*, 3655. [[CrossRef](#)]
12. Zhang, H.; Liu, J.; Du, L.; Ma, C.; Leung, N.L.C.; Niu, Y.; Qin, A.J.; Peng, S.Q.; Sung, H.H.Y.; Williams, I.D.; et al. Drawing a clear mechanistic picture for the aggregation-induced emission process. *Mater. Chem. Front.* **2019**, *3*, 1143. [[CrossRef](#)]
13. Liu, S.; Zhou, X.; Zhang, H.; Ou, H.; Lam, J.W.Y.; Liu, Y.; Shi, L.; Ding, D.; Tang, B.Z. Molecular Motion in Aggregates: Manipulating TICT for Boosting Photothermal Theranostics. *J. Am. Chem. Soc.* **2019**, *141*, 5359. [[CrossRef](#)] [[PubMed](#)]
14. Luo, W.; Tan, Y.; Gui, Y.; Yan, D.; Wang, D.; Tang, B.Z. Near-Infrared-Emissive AIE Bioconjugates: Recent Advances and Perspectives. *Molecules* **2022**, *27*, 3914. [[CrossRef](#)]
15. Jiang, N.; Shen, T.; Sun, J.Z.; Tang, B.Z. Aggregation-induced emission: Right there shining. *Sci. China Mater.* **2019**, *62*, 1227. [[CrossRef](#)]
16. Chen, C.; Ni, X.; Jia, S.R.; Liang, Y.; Wu, X.L.; Kong, D.L.; Ding, D. Massively Evoking Immunogenic Cell Death by Focused Mitochondrial Oxidative Stress using an AIE Luminogen with a Twisted Molecular Structure. *Adv. Mater.* **2019**, *31*, 1904914. [[CrossRef](#)]
17. Wang, X.; Zhang, L.; Li, Q.; Gao, Y. A novel dark resonance energy transfer-based fluorescent probe with large Stokes shift for the detection of pH and its imaging application. *Dye. Pigment.* **2020**, *181*, 108614. [[CrossRef](#)]
18. Zhao, Q.; Zhang, S.; Liu, Y.; Mei, J.; Chen, S.; Lu, P.; Qin, A.; Ma, Y.; Sun, J.Z.; Tang, B.Z. Tetraphenylethenyl-modified perylene bisimide: Aggregation-induced red emission, electrochemical properties and ordered microstructures. *J. Mater. Chem.* **2012**, *22*, 7387. [[CrossRef](#)]
19. Zhang, J.; Ma, S.; Fang, H.; Xu, B.; Sun, H.; Chan, I.; Tian, W. Insights into the Origin of Aggregation Enhanced Emission of 9, 10-Distyrylanthracene Derivatives. *Mater. Chem. Front.* **2017**, *1*, 1422. [[CrossRef](#)]
20. Meti, P.; Yang, J.W.; Gong, Y.D. Aggregation induced emission properties of cruciform-type conjugated pyrazine molecules with four pendent donor groups. *Dye. Pigment.* **2021**, *192*, 109419. [[CrossRef](#)]
21. Guo, Z.; Yan, C.; Zhu, W.H. High-Performance Quinoline-Malononitrile Core as a Building Block for the Diversity-Oriented Synthesis of AIEgens. *Angew. Chem. Int. Ed.* **2020**, *59*, 9812. [[CrossRef](#)] [[PubMed](#)]
22. Tonga, M. Regulation of aggregation-induced emission color of α -cyanostilbene luminogens through donor engineering of amino derivatives. *Tetrahedron Lett.* **2021**, *69*, 152972. [[CrossRef](#)]
23. Liu, C.C.; Yang, J.C.; Lam, J.W.; Feng, H.T.; Tang, B.Z. Chiral assembly of organic luminogens with aggregation-induced emission. *Chem. Sci.* **2022**, *13*, 611. [[CrossRef](#)] [[PubMed](#)]
24. Li, M.Q.; Zhu, W.H. Sterically Hindered Diarylethenes with a Benzobis(thiadiazole) Bridge: Enantiospecific Transformation and Reversible Photosuperstructures. *Acc. Chem. Res.* **2022**, *55*, 3136. [[CrossRef](#)] [[PubMed](#)]
25. Sun, Y.Q.; Lei, Z.Q.; Ma, H.C. Twisted aggregation-induced emission luminogens (AIEgens) contribute to mechanochromism materials: A review. *J. Mater. Chem. C* **2022**, *10*, 14834. [[CrossRef](#)]
26. Fan, D.Y.; Wang, D.; Han, T.; Tang, B.Z. Fused Heterocyclic Polymers with Aggregation-Induced Emission: Synthesis and Applications. *ACS Appl. Polym. Mater.* **2022**, *4*, 3120. [[CrossRef](#)]

27. Yang, Z.; Ge, X.Y.; Li, W.L.; Mao, Z.; Chen, X.J.; Xu, C.; Gu, F.L.; Zhang, Y.; Zhao, J.; Chi, Z.G. From *para* to *ortho*: Incarnating conventional TADF molecules into AIE-TADF molecules for highly-efficient non-doped OLEDs. *Chem. Eng. J.* **2022**, *442*, 136219. [[CrossRef](#)]
28. Sun, H.; Tang, X.X.; Zhang, R.; Sun, W.H.; Miao, B.X.; Zhao, Y.; Ni, Z.H. Tetraphenylethene-substituted benzothiadiazoles: AIE and TICT properties, tunable intramolecular conjugation and application in detecting trace water in organic solvents. *Dye. Pigment.* **2020**, *174*, 108051. [[CrossRef](#)]
29. Jia, J.H.; Wu, L.Y. Reversible fluorescent switching properties of pyrene-substituted acylhydrazone derivatives toward mechanical force and acid vapor with aggregation-induced emission. *J. Photochem. Photobiol. A* **2020**, *399*, 112640. [[CrossRef](#)]
30. Jia, J.; Wen, J. Multi-stimuli responsive fluorescence switching of D-A tetraphenylethylene functionalized cyanopyridine isomers. *Tetrahedron Lett.* **2020**, *61*, 151577. [[CrossRef](#)]
31. Pratihari, S.; Bhattacharyya, A.; Prasad, E. Achieving ACQ-AIE modulation using isostructural organic fluorophores. *J. Photochem. Photobiol. A* **2020**, *396*, 112458. [[CrossRef](#)]
32. Dong, P.-P.; Liu, Y.-Y.; Peng, Q.-C.; Li, H.-Y.; Li, K.; Zang, S.-Q.; Tang, B.Z. Luminescent MOFs constructed by using butterfly-like AIE ligands. *Dalton Trans.* **2023**, *52*, 1913. [[CrossRef](#)] [[PubMed](#)]
33. Ahangar, A.A.; Bhat, I.A.; Dar, A.A.A. AIE in the Halogenated Anils and their Utilization as Fluorescent Probes for Explosive Nitro-aromatics. *New J. Chem.* **2023**, *47*, 4775. [[CrossRef](#)]
34. Wang, D.X.; Tang, L.H.; Wang, J.J.; Zheng, Z.; Cai, H.M.; Li, L.C.; Gan, X.P.; Zhou, H.P. Three polarity-sensitive fluorescence probe possessing AIE activity and its application on lipid droplets imaging. *Dye. Pigment.* **2023**, *211*, 111082. [[CrossRef](#)]
35. Miao, X.R.; Cai, Z.K.; Zou, H.Q.; Li, J.X.; Zhang, S.Y.; Ying, L.; Deng, W.L. Achieving halogen bonding enhanced ultra-highly efficient AIE and reversible mechanochromism properties of TPE-based luminogens: Position of bromine substituents. *J. Mater. Chem. C* **2022**, *10*, 8390. [[CrossRef](#)]
36. Shellaiah, M.; Sun, K.-W. Pyrene-Based AIE Active Materials for Bioimaging and Theranostics Applications. *Biosensors* **2022**, *12*, 550. [[CrossRef](#)] [[PubMed](#)]
37. Wang, X.; Lin, X.; Li, R.; Wang, Z.; Liu, W.; Chen, L.; Chen, N.; Dai, T.; Sun, S.; Li, Z.; et al. Achieving Molecular Fluorescent Conversion from Aggregation-Caused Quenching to Aggregation-Induced Emission by Positional Isomerization. *Molecules* **2022**, *27*, 193. [[CrossRef](#)]
38. Yan, L.Q.; Li, R.J.; Shen, W.; Qi, Z.J. Multiple-color AIE coumarin-based Schiff bases and potential application in yellow OLEDs. *J. Lumin.* **2018**, *194*, 151. [[CrossRef](#)]
39. Ekbote, A.; Han, S.H.; Jadhav, T.; Mobin, S.M.; Lee, J.Y.; Misra, R. Stimuli responsive AIE active positional isomers of phenanthroimidazole as non-doped emitters in OLEDs. *J. Mater. Chem. C* **2018**, *6*, 2077. [[CrossRef](#)]
40. Jiang, W.; Zhou, R.Y.; Zhao, G.M.; Ma, D.Y.; Chen, H.W.; Zhang, Z.M.; Tian, W.W.; Sun, Y.M. Isomer engineering to adjusting full width at half maximum and emission wavelength for efficient solution-processed red OLEDs. *Opt. Mater.* **2023**, *136*, 113505. [[CrossRef](#)]
41. Kim, B.-G.; Chung, K.; Kim, J. Molecular Design Principle of All-organic Dyes for Dye-Sensitized Solar Cells. *Chem. A Eur. J.* **2013**, *19*, 5220. [[CrossRef](#)] [[PubMed](#)]
42. Balasaravanan, R.; Duraimurugan, K.; Sivamani, J.; Thiagarajan, V.; Siva, A. Synthesis and photophysical properties of triphenylamine-based multiply conjugated star-like molecules. *New J. Chem.* **2015**, *39*, 7472. [[CrossRef](#)]
43. Sun, H.; Liu, D.; Wang, T.; Lu, T.; Li, W.; Ren, S.; Hu, W.; Wang, L.; Zhou, X. Enhanced internal quantum efficiency in dye-sensitized solar cells: Effect of long-lived charge-separated state of sensitizers. *ACS Appl. Mater. Interfaces* **2017**, *9*, 9880. [[CrossRef](#)] [[PubMed](#)]
44. Lu, T.; Sun, H.; Colley, N.D.; Bridgman, C.N.; Liu, D.; Li, W.; Hu, W.; Zhou, X.; Wang, T.; Wang, L. Tuning the donors to control the lifetimes of charge-separated states in triazine-based donor-acceptor systems. *Dye. Pigment.* **2017**, *136*, 404. [[CrossRef](#)]
45. Jana, P.; Paramasivam, M.; Khandelwal, S.; Dutta, A.; Kanvah, S. Perturbing the AIEE activity of pyridine functionalized a-cyanostilbenes with donor substitutions: An experimental and DFT study. *New J. Chem.* **2020**, *44*, 218. [[CrossRef](#)]
46. Chen, M.; Chen, R.; Shi, Y.; Wang, J.; Cheng, Y.; Li, Y.; Gao, X.; Yan, Y.; Sun, J.Z.; Qin, A.J.; et al. Malonitrile-Functionalized Tetraphenylpyrazine: Aggregation-Induced Emission, Ratiometric Detection of Hydrogen Sulfide, and Mechanochromism. *Adv. Funct. Mater.* **2018**, *28*, 1704689. [[CrossRef](#)]
47. Qian, J.; Tang, B.Z. AIE Luminogens for Bioimaging and Theranostics: From Organelles to Animals. *Chem* **2017**, *3*, 56. [[CrossRef](#)]
48. Yang, Y.; Xiao, R.; Cao, X.; Chen, Z.; Lv, X.; Zhang, Y.; Gong, S.; Zou, Y.; Yang, C. Phenoxazine-Dibenzothiophene Sulfoximine Emitters Featuring Both Thermally Activated Delayed Fluorescence and Aggregation Induced Emission. *Molecules* **2021**, *26*, 5243. [[CrossRef](#)]
49. Yin, W.; Li, Y.; Li, N.; Yang, W.; An, H.; Gao, J.; Bi, Y.; Zhao, N. Hybridization of Triphenylamine and Salicylaldehyde: A Facile Strategy to Construct Aggregation-Induced Emission Luminogens with Excited-State Intramolecular Proton Transfer for Specific Lipid Droplets and Gram-Positive Bacteria Imaging. *Adv. Opt. Mater.* **2020**, *8*, 1902027. [[CrossRef](#)]
50. Wang, Y.J.; Shi, Y.; Wang, Z.; Zhu, Z.; Zhao, X.; Nie, H.; Qian, J.; Qin, A.J.; Sun, J.Z.; Tang, B.Z. A Red to Near-IR Fluorogen: Aggregation-Induced Emission, Large Stokes Shift, High Solid Efficiency and Application in Cell-Imaging. *Chem. A Eur. J.* **2016**, *22*, 9784. [[CrossRef](#)]
51. Tebyetekerwa, M.; Cheng, Y.; Zhang, J.; Li, W.; Li, H.; Neupane, G.P.; Wang, B.; Truong, T.N.; Xiao, C.; Al-Jassim, M.M.; et al. Emission Control from Transition Metal Dichalcogenide Monolayers by Aggregation-Induced Molecular Rotors. *ACS Nano* **2020**, *14*, 7444. [[CrossRef](#)] [[PubMed](#)]

52. Frisch, M.J.; Trucks, G.W.; Schlegel, H.B.; Scuseria, G.E.; Robb, M.A.; Cheeseman, J.R.; Scalmani, G.; Barone, V.; Mennucci, G.A.; Petersson, G.A.; et al. *Gaussian 09*; Gaussian, Inc.: Wallingford, CT, USA, 2009. Available online: <https://gaussian.com/glossary/g09/> (accessed on 1 March 2023).
53. Ge, F.S.; Xu, F.; Gong, K.; Liu, D.Z.; Li, W.; Wang, L.C.; Zhou, X.Q. Sensitizers designed toward efficient intramolecular charge separation for p-type dye-sensitized solar cells. *Dye. Pigment.* **2022**, *200*, 110127. [[CrossRef](#)]
54. Mathew, S.; Yella, A.; Gao, P.; Humphry-Baker, R.; Curchod, B.F.E.; Ashari-Astani, N.; Tavernelli, I.; Rothlisberger, U.; Nazeeruddin, M.K.; Grätzel, M. Dye-sensitized solar cells with 13% efficiency achieved through the molecular engineering of porphyrin sensitizers. *Nat. Chem.* **2014**, *6*, 242. [[CrossRef](#)]
55. Bredas, J.-L. Mind the gap! *Mater. Horiz.* **2014**, *1*, 17. [[CrossRef](#)]
56. Ma, C.P.; He, J.J.; Xu, B.J.; Xie, G.Y.; Xie, Z.L.; Mao, Z.; Chi, Z.G. A TPE-benzothiazole piezochromic and acidichromic molecular switch with high solid state luminescent efficiency. *RSC Adv.* **2018**, *8*, 6252. [[CrossRef](#)]
57. Sun, H.; Sun, R.; Sun, J.; Gao, J.; Liu, R.; Zhu, Y.; Liu, D.; Liu, Z.; Zeng, J.; Zhu, Y.; et al. Donor-Acceptor structured phenylmethylene pyridineacetonitrile derivative with aggregation-induced emission characteristics: Photophysical, mechanofluorochromic and electroluminescent properties. *J. Mol. Struct.* **2022**, *1262*, 132957. [[CrossRef](#)]
58. Liu, X.; Wei, X.; Miao, Y.; Tao, P.; Wang, H.; Xu, B. Triphenylamine-based small molecules with aggregation-induced emission and mechanochromic luminescence properties for OLED application. *Tetrahedron* **2021**, *86*, 132061. [[CrossRef](#)]
59. Martínez-Abadía, M.; Giménez, R.; Ros, M.B. Self-Assembled α -Cyanostilbenes for Advanced Functional Materials. *Adv. Mater.* **2018**, *30*, 1704161. [[CrossRef](#)]
60. Dong, Y.; Qian, J.; Liu, Y.; Zhu, N.; Xu, B.; Ho, C.-L.; Tian, W.; Wong, W.-Y. Imidazole-containing cyanostilbene-based molecules with aggregation-induced emission characteristics: Photophysical and electroluminescent properties. *New J. Chem.* **2019**, *43*, 1844. [[CrossRef](#)]

Disclaimer/Publisher's Note: The statements, opinions and data contained in all publications are solely those of the individual author(s) and contributor(s) and not of MDPI and/or the editor(s). MDPI and/or the editor(s) disclaim responsibility for any injury to people or property resulting from any ideas, methods, instructions or products referred to in the content.